A Class of Nonhydrostatic Global Models

PIOTR K. SMOLARKIEWICZ

National Center for Atmospheric Research, Boulder, Colorado

LEN G. MARGOLIN

CNLS, Los Alamos National Laboratory, Los Alamos, New Mexico

ANDRZEJ A. WYSZOGRODZKI

Department of Physics,
University of Warsaw, Warsaw, Poland, and
National Center for Atmospheric Research, Boulder, Colorado

(Manuscript received 13 May 1999, in final form 23 June 2000)

ABSTRACT

A Cartesian, small- to mesoscale nonhydrostatic model is extended to a rotating mountainous sphere, thereby dispensing with the traditional geophysical simplifications of hydrostaticity, gentle terrain slopes, and weak rotation. The authors discuss the algorithmic design, relative efficiency, and accuracy of several different variants (hydrostatic, nonhydrostatic, implicit, explicit, elastic, anelastic, etc.) of the global model and prepare the ground for a future ''global cloud model''—a research tool to study effects of small- and mesoscale phenomena on global flows and vice versa. There are two primary threads to the discussion: (a) presenting a novel semi-implicit anelastic global dynamics model as it naturally emerges from a small-scale dynamics model, and (b) demonstrating that nonhydrostatic anelastic global models derived from small-scale codes adequately capture a broad range of planetary flows while requiring relatively minor overhead due to the nonhydrostatic formulation of the governing equations. The authors substantiate their theoretical discussions with a detailed analysis of numerous simulations of idealized global orographic flows and climate states.

1. Introduction

In this paper we describe the extension of a small- to mesoscale nonhydrostatic model to global scales. Traditionally, numerical models for simulating planetary-scale weather and climate employ the hydrostatic primitive equations—a truncated form of Navier–Stokes' equations that neglects vertical accelerations and uses simplified Coriolis forces.[1] Although there is no evidence so far that including nonhydrostatic effects in global models has any physical significance for large-scale solutions, there is an emerging trend in the community toward restoring the Navier–Stokes' equations (or at least their less constrained forms) in global models of atmospheres and oceans. The primary motivation is that state-of-the-art computers already admit resolutions where local nonhydrostatic effects become noticeable. Other advantages include: the convenience of local mesh refinement, better overall accuracy while entailing insubstantial computational overhead relative to hydrostatic models, generality and the resulting convenience of maintaining a single large code, the theoretical well-posedness in the continuous limit (Oliger and Sundström 1978), conceptual simplicity and mathematical elegance—features important for education and dissemination.

The few existing nonhydrostatic global models differ in their analytic formulation and numerical design, reflecting their different origins and purposes. The compressible atmospheric models of Semazzi et al. (1995) and Cullen et al. (1997) aim at high-resolution numerical weather prediction (NWP) and extend approximation methods traditional in NWP on nonhydrostatic dynamics. The incompressible Boussinesq model of Marshall et al. (1997a) extends a convection-scale stratified-fluid model to a flexible research tool for all-scale studies of oceanic circulations. The development in this paper is philosophically akin to that in Marshall et al. (1997a) but addresses atmospheric circulations.

[1] For a thorough critique of the hydrostatic primitive equations see Marshall et al. (1997b).

Corresponding author address: Piotr K. Smolarkiewicz, NCAR/MMM, P.O. Box 3000, Boulder, CO 80307-3000.
E-mail: smolar@ncar.ucar.edu

Much of our recent research (Anderson et al. 1997; Smolarkiewicz and Margolin 1997) has aimed to improve the design of our high-performance numerical solver for simulating flows of moist (and precipitating), rotating, stratified fluids past a specified time-dependent irregular lower boundary. This model is representative of a class of small-scale nonhydrostatic atmospheric codes that employ the anelastic equations of motion in a terrain-following curvilinear framework. A unique feature of our model is the parallel implementations of nonoscillatory forward-in-time (NFT) semi-Lagrangian and Eulerian approximations (Smolarkiewicz and Pudykiewicz 1992; Smolarkiewicz and Margolin 1993), options that are selectable by the user. This approach has been employed in a variety of small- and mesoscale geophysical applications and the quality of results suggest that NFT methods are superior to the more traditional centered-in-time-and-space schemes in terms of accuracy, computational efficiency, flexibility, and robustness (cf. Smolarkiewicz and Margolin 1997, 1998).

The goal of this study is to prepare the ground for a future ''global cloud model''—a research tool to investigate effects of small- and mesoscale phenomena on global flows and vice versa. In order to arrive at an optimal design, we explore several extensions of our small-scale NFT model to a mountainous sphere. Each of the resulting global models naturally dispenses with the traditional simplifications of hydrostaticity, gentle terrain slopes, and weak rotation. However, not all possible extensions are practical. For example, straightforward extensions that account only for the appropriate metric coefficients, forces, and boundary conditions inevitably lead to computationally intractable global models of the earth's meteorology. The key issue is the formulation and efficient solution of the elliptic equations that arise in nonhydrostatic modeling.

One consequence of nonhydrostatic modeling using either filtered equations or implicit discretization methods, is the necessity of solving a full 3D Poisson or Helmholtz equation, which typically does not possess the regularity properties that allow the use of fast standard methods. The condition number (of the elliptic operator) grows in proportion to the square of the horizontal scale of the model, and so does the degree of difficulty in solving the problem. All published works on existing nonhydrostatic global models (cf. Cullen et al. 1997; Marshall et al. 1997a; Semazzi et al. 1995) note the importance of this key issue. Because NFT methods are inherently two-time-level, an accurate (i.e., time-centered) integration of forces complicates the problem even further, leading ultimately to the inversion of a large nonsymmetric linear system that represents a complex nonself-adjoint 3D elliptic partial differential equation for pressure. For deep fluids, such a problem can be solved easily using standard Krylov subspace methods for nonsymmetric operators (Smolarkiewicz and Margolin 1994; Smolarkiewicz et al. 1997). For shallow fluids typical of the earth's meteorology, however, the resulting elliptic operator is extremely stiff,[2] necessitating additional enhancements to the Krylov solvers to assure convergence. We will compare two strategies in this paper. One is to use the hydrostatic solution for pressure as an initial guess for the iterative nonhydrostatic pressure solver. This approach naturally facilitates the optional implementation of hydrostatic or nonhydrostatic models (cf. Marshall et al. 1997a). The second strategy dispenses with the decomposition of the pressure into a hydrostatic and a nonhydrostatic part but relies on effective preconditioners for the Krylov solver. This results in a simpler, more general, and elegant variant of the model. Yet the most important benefit of the latter variant is the ease of further extension to the semi-implicit (with respect to the internal gravity waves)[3] NFT scheme [see the appendix for a formal exposition; for a complete technical development, see appendix B in Smolarkiewicz et al. (1999)].

We present our nonhydrostatic anelastic semi-implicit global NFT model as it emerges from a series of sequential extensions of a small-scale dynamics model. Using benchmark ''dynamical core'' experiments that idealize weather and climate simulations (while excluding moist processes, radiation, and subgrid-scale turbulence schemes), we compare the relative accuracy and efficiency of hydrostatic, nonhydrostatic, implicit, explicit, semi-Lagrangian, Eulerian, elastic, anelastic, incompressible, etc., variants of the global model. We measure the differences due to analytic formulation of the governing equations against the truncation errors of legitimate optional second-order-accurate discretization approximations. This analysis builds our confidence that nonhydrostatic anelastic global models derived from small-scale codes (i.e., not relying on large-scale balances in their analytic/numerical design) adequately capture a broad range of planetary flows while requiring relatively minor overhead due to the nonhydrostatic formulation.

The numerical models considered in this study have been developed over several years; some were abandoned as impractical, while others have been pursued and generalized. To aid the reader's orientation in the discussions that follow, we list all models in a historical order and characterize them briefly in Table 1.

2. Model description

In this paper, we focus on an inviscid, adiabatic, density-stratified fluid whose undisturbed, geostrophically balanced ''ambient'' (or ''environmental'') state is described by the potential temperature $\Theta_e = \Theta_e(\mathbf{x})$ and the velocity $\mathbf{v}_e = \mathbf{v}_e(\mathbf{x})$. The expanded form of the governing anelastic equations used in the model, which ac-

[2] A fair estimate of the spectral condition number is $\kappa \sim O(10^{10})$.

[3] In all models discussed in this paper, the external mode is eliminated by assuming a rigid-lid upper boundary.

TABLE 1. Models considered in this study. The first column refers to the governing fluid equations. The second column distinguishes between explicit or implicit treatment of internal gravity waves. The third column distinguishes between semi-Lagrangian (SL) and Eulerian (EU) options of the model algorithm. The fourth column identifies the means of accelerating the Krylov solver for the elliptic pressure equation.

Equations	GW integration	LE operator	Solver acceleration
Anelastic nonhydrostatic	Explicit	SL	None/diagonal preconditioner
Anelastic hydr./nonhydr.	Explicit	SL	Hydrostatic first guess
Anelastic nonhydrostatic	Explicit	SL	ADI preconditioner
Elastic nonhydrostatic	Explicit	SL	ADI preconditioner
Incompressible Euler	Explicit	SL	ADI preconditioner
Anelastic nonhydrostatic	Implicit	SL/EU	ADI preconditioner

counts for the coordinate transformations, has been given in Smolarkiewicz et al. (1998, 1999) closely following Clark et al. 1996.[4] To facilitate further discussion on alternate model formulations, here we present only compact, symbolic forms of the governing equations. We start with the anelastic system of Lipps and Hemler 1982 (see also Lipps 1990):

$$\frac{\mathcal{D}\mathbf{v}}{\mathcal{D}t} = -\mathrm{Grad}\left(\frac{p'}{\overline{\rho}}\right) + \mathbf{g}\frac{\Theta'}{\overline{\Theta}} - \mathbf{f}\times\mathbf{v}' + \mathcal{M}', \quad (1)$$

$$\frac{\mathcal{D}\Theta}{\mathcal{D}t} = 0, \quad (2)$$

$$\mathrm{Div}(\overline{\rho}\mathbf{v}) = 0. \quad (3)$$

Here the operators $\mathcal{D}/\mathcal{D}t$, Grad, and Div have their usual meaning of material derivative, gradient, and divergence; $\mathbf{v}$ denotes the velocity vector;[5] $\mathcal{M}$ symbolizes appropriate metric forces [Christoffel terms proportional to products of velocity components; see Smolarkiewicz et al. (1998, 1999)]; Θ, ρ, and p denote potential temperature, density, and pressure; $\mathbf{f}$ and $\mathbf{g}$ symbolize the vectors of the ''Coriolis parameter'' and gravity, respectively. Primes denote deviations from the ambient state, and overbars refer to the horizontally homogeneous hydrostatic reference state of the Boussinesq expansion around a constant stability profile [see section 2b in Clark and Farley (1984) for a discussion].

The anelastic equations (1)–(3) may be viewed as combining two distinct approximations in the compressible Euler equations: the Boussinesq type linearization of the pressure gradient forces and mass fluxes in, correspondingly, (1) and (3); and the anelasticity per se equivalent to taking the limit of an infinite speed of sound. To assess the impact of both assumptions inherent in the anelastic system we employ, respectively, the fully incompressible Euler equations and a Boussinesq elastic system. Using the same notation as in (1)–(3), the incompressible Euler equations are written as follows

$$\frac{\mathcal{D}\mathbf{v}}{\mathcal{D}t} = -\frac{1}{\rho}\mathrm{Grad}(p') - \mathbf{g}\frac{\rho'}{\rho} - \mathbf{f}\times\mathbf{v}' + \mathcal{M}', \quad (4)$$

$$\frac{\mathcal{D}\rho}{\mathcal{D}t} = 0, \quad (5)$$

$$\mathrm{Div}(\mathbf{v}) = 0. \quad (6)$$

The elastic Boussinesq model consists of the momentum and entropy equations (1) and (2), formally identical with those of the anelastic system, and the mass continuity equation

$$\frac{\partial}{\partial t}\left(\frac{p'}{\overline{\rho}}\right) + \frac{c_s^2}{\overline{\rho}}\mathrm{Div}(\overline{\rho}\mathbf{v}) = 0, \quad (7)$$

where c_s is the speed of sound (constant to the Boussinesq approximation, taken here to be 300 m s^{-1}). Technically, the conversion from the anelastic to incompressible equations is achieved easily within the framework of the explicit numerical model (entry 3 in Table 1), by redefining the pressure gradient forces and buoyancy, and by equivalencing the Θ field to the fluid density $\rho(\mathbf{x}, t)$ (cf. Rotunno and Smolarkiewicz 1995). The conversion to the elastic Boussinesq system is a particularly simple alteration of the model (either explicit or implicit), merely requiring replacement of the anelastic mass continuity equation (3) with (7). In effect, the Poisson equation for pressure (A5) is transformed into a slightly better-conditioned Helmholtz equation (A7); see the appendix for discussions.

Our basic NFT approach for approximating integrals of the governing equations on a discrete mesh is second-order-accurate in space and time. The two optional model algorithms, semi-Lagrangian (Smolarkiewicz and Pudykiewicz 1992) and Eulerian (Smolarkiewicz and Margolin 1993), correspond to the trajectory-wise and pointwise integrals of the evolution equations (1, 2) or (4, 5). All variables are defined at the same grid points $\mathbf{x}_i$—a choice important for the efficacy of the unified semi-Lagrangian–Eulerian NFT approach (Smolarkiewicz and Margolin 1997). The theory underlying the NFT

[4] The anelastic model on a mountainous globe results from a composition of two mappings: it can be derived by transforming the anelastic variant of the Navier–Stokes' equations on a rotating sphere (Gill 1982; Dutton 1986) to a standard terrain-following coordinates (Gal-Chen and Somerville 1975).

[5] We employ the standard representation where components of $\mathbf{v}$ are defined in terms of a local tangent Cartesian framework aligned with standard geographical coordinates.

numerical algorithms has been documented in earlier works, and their basic properties of computational stability, accuracy, and efficiency are already established. In this paper we focus on the overall design of nonhydrostatic NFT models and their relative performance in representative complex planetary flow problems.

We write the resulting finite-difference approximations in the compact form

$$\psi_{\mathbf{i}}^{n+1} = \mathrm{LE}_{\mathbf{i}}(\tilde{\psi}) + 0.5\Delta t \mathbf{F}_{\mathbf{i}}^{n+1}. \tag{8}$$

Here, LE denotes either an advective semi-Lagrangian or a flux-form Eulerian NFT transport operator [sections 3.1 and 3.2 in Smolarkiewicz and Margolin (1997), respectively];[6] $\tilde{\psi} \equiv \psi^n + 0.5\Delta t \mathbf{F}^n$, where the indices **i** and n denote the spatial and temporal location on a (logically) rectangular Cartesian mesh. Transporting the auxiliary field $\tilde{\psi}$ (rather than the fluid variable alone) has been shown to be important for the accuracy and stability of forward-in-time approximations. In the Eulerian algorithm, transporting $\tilde{\psi}$ is a consequence of compensating the first-order truncation error proportional to the divergence of the advective flux of **F**, while in the semi-Lagrangian algorithm it derives straightforwardly from the trapezoidal-rule approximation for the integral on the right-hand side (rhs) of the evolution equations; see Smolarkiewicz and Margolin (1997, 1993), for further discussions.

Equation (8) represents a system implicit with respect to the dependent variables (e.g., Θ and components of **v**). Completion of the model algorithm requires a straightforward algebraic inversion of (8), resulting in the formulation of the boundary value problem for pressure implied by the mass continuity constraint—for example, Eq. (3). In the appendix, we outline the essential steps of this fairly standard projection procedure and focus on key features of the different numerical models considered. The resulting elliptic equations are solved, subject to appropriate boundary conditions, using a conjugate-gradient method. We have found the generalized conjugate-residual (GCR) approach of Eisenstat et al. (1983)—a nonsymmetric Krylov solver akin to the celebrated GMRES algorithm (Saad and Schultz 1986)—especially convenient for geophysical fluid models. Further technical details of the projection procedure, an explicit form of the resulting elliptic operator for the anelastic system, and a description of the complete preconditioned Krylov solver can be found in Smolarkiewicz et al. (1999).

[6] Specifically, the semi-Lagrangian algorithm remaps transported fields to the departure points of flow trajectories arriving at grid points $(\mathbf{x}_{\mathbf{i}}, t^{n+1})$ (Smolarkiewicz and Grell 1992), while the Eulerian scheme integrates the homogeneous transport equation $\overline{\rho}\tilde{\psi}_t + \mathrm{Div}(\overline{\rho}\mathbf{v}\tilde{\psi}) = 0$ (Smolarkiewicz and Clark 1986); both methods preserve sign and monotonicity of the transported variables.

3. Results

In this section we analyze in detail two examples of idealized global flows. These are representative of two distinct classes of application—basic geophysical fluid dynamics of a mechanically forced *laminar* system, and climate studies of a thermally forced *turbulent* system. These examples serve as convenient test beds for the overall accuracy (both analytic and numerical) and relative performance of our nonhydrostatic global models. Note that the overall intent of our analysis is not to demonstrate that our small-scale code works well at resolutions appropriate for nonhydrostatic dynamics (this is well documented in the literature already), but, to the contrary, to demonstrate that the globally extended small-scale models adequately capture a broad range of large-scale responses even though they do not exploit global balances in their analytic–numerical design.

a. Orographic flow

The first problem is an orographic flow of a shallow fluid on a rotating sphere. It was proposed by Williamson et al. (1992) for evaluating the accuracy and efficiency of numerical methods for global-scale dynamics and has become a benchmark in the field. Its original formulation is in terms of the shallow water equations. Here, we extend this problem to a continuously stratified 3D Boussinesq fluid while keeping other flow parameters consistent with the benchmark. We use the Boussinesq option of the anelastic model to enable meaningful comparisons of the three governing systems (1–3), (4–6), and (1, 2, 7). In this manner, we can quantify the effects of the non-Boussinesq baroclinicity and finite speed of sound relative to the truncation errors of finite-difference approximations. We anticipate these results would extrapolate to similar comparisons of the anelastic and fully compressible Euler equations.

Figure 1 shows the pattern of vertical and meridional velocity components after 15 days of simulated zonal flow of a stratified Boussinesq fluid past a large hill (consistent with the linear solution of Grose and Hoskins 1979; cf. their Fig. 3a) using the semi-Lagrangian implicit variant of the model discussed above. The flow parameters are

$$u_e = \hat{U}(r')\cos\phi, \qquad v_e = 0, \qquad \hat{U}(r') = U_o\Gamma,$$
$$U_o = 20 \text{ m s}^{-1}; \tag{9}$$

and the corresponding thermally balanced state

$$\Theta_e = \hat{\Theta}_e(r') + \frac{\overline{\Theta}}{g}\sin^2\phi\left[\frac{\hat{U}^2}{\Gamma R} + 2\Omega\hat{U} - \frac{1}{2}\frac{\partial}{\partial r}(\hat{U}^2 + 2\Omega\hat{U}\Gamma R)\right], \tag{10}$$

where $\hat{\Theta}_e(r') = \Theta_o[1 + r'N^2/g]$, and the Brunt–Väisälä

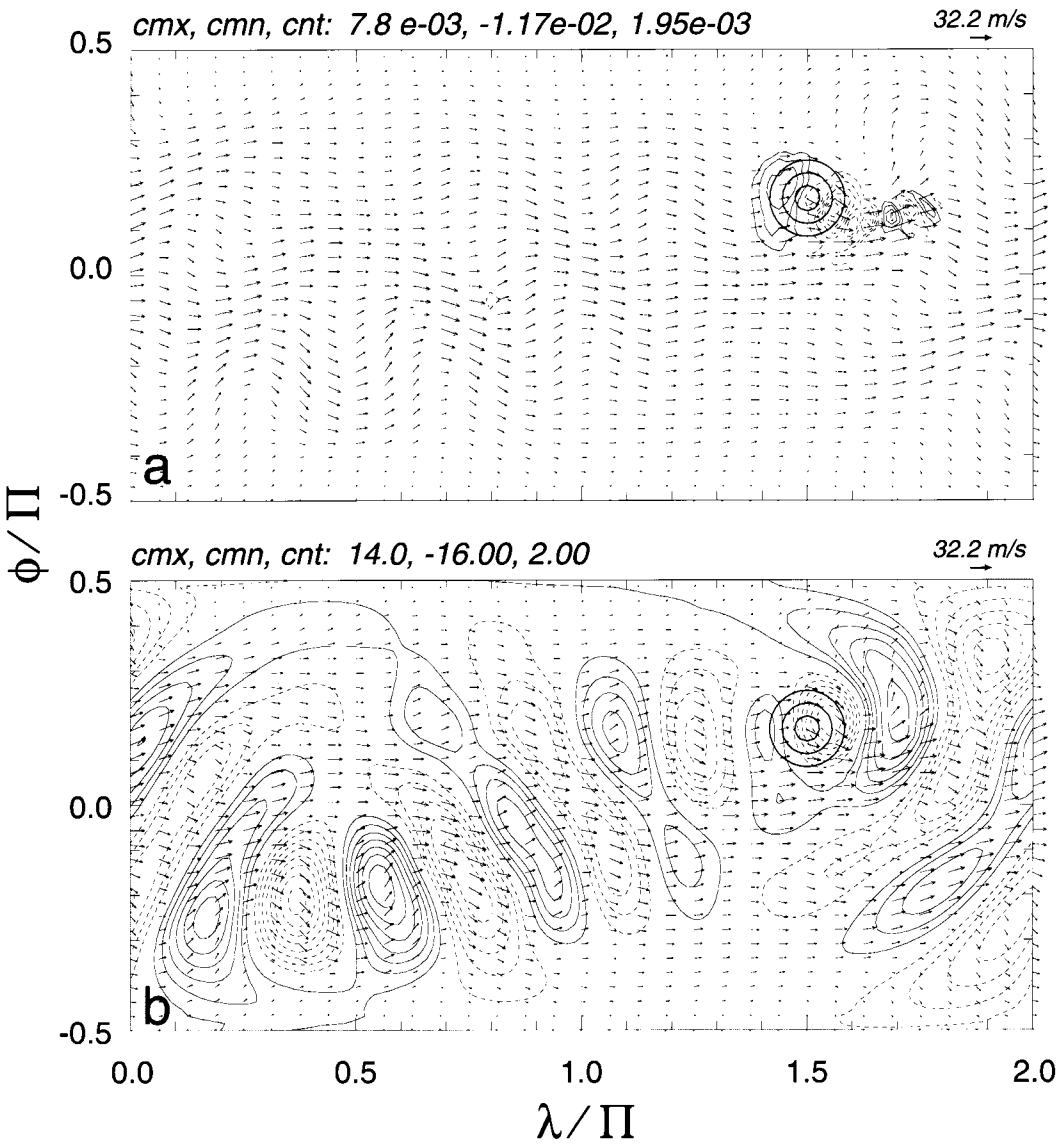

FIG. 1. Planetary wave propagation on a sphere. Contours show patterns of (a) vertical and (b) meridional velocity components in m s^{-1}, with imposed flow vectors, at 4 km after 15 days of simulation. Contour maxima (cmx), minima (cmn), and intervals (cnt) are shown in the upper-left corner of each panel. Negative values are dashed, and zero contours are omitted. The mountain is illustrated with thick solid circles. Maximum vector lengths (here identical) are shown in the upper-right corner of each plate.

frequency $N = 10^{-2}$ s^{-1}. Here r, R, ϕ, and Ω denote, respectively, the radial component of the vector radius, sphere's radius, latitude, and angular velocity of the planetary rotation. Also, $\Gamma \equiv r/R$, and $r' \equiv r - R$. The conical hill with height 2×10^3 m and base radius $\Pi/9$ (in terms of lat–long) is centered at $(\lambda, \phi) = (3\Pi/2, \Pi/6)$, where λ is the longitude. The globe is covered with a uniform spherical mesh with $nx \times ny = 128 \times 64$ grid intervals (no grid points at the poles) and the $H = 8 \times 10^3$ m deep atmosphere is resolved with $nz = 20$ uniform grid intervals. The time step $\Delta t = 7.2 \times 10^3$ s.

The simulation in Fig. 1 employs no viscous filters and remains, effectively, inviscid. The residual dissipation due to the nonoscillatory remapping algorithm (Smolarkiewicz and Grell 1992) suffices merely to preserve monotonicity of the transported variables [consistent with analytic properties of fundamental conservation laws; Smolarkiewicz and Pudykiewicz (1992), see also section 2d in Prusa et al. (1996), and Margolin et al. (1999), for further discussions]. For reference, the execution time on a single processor CRAY J-90 is ~1.4 $\times 10^4$ s. This value can be easily reduced by a factor of about 2 by using dissipative filters in the polar regions (a common practice in global circulation models). With the large time step employed here, most of the com-

TABLE 2. Comparison of various simulations of the 15-day evolution of the orographic flow on the sphere. The first column numbers runs for later reference. The second column lists the solver (e.g., Eulerian vs semi-Lagrangian, hydrostatic vs nonhydrostatic, explicit vs implicit, etc.; see the text for details) and the time step (Δt in s) employed. Columns 3–6 provide norms of the meridional and vertical velocity components (in m s^{-1}), respectively. The last column lists single-processor Cray J90 CPU times (min).

Run	Solver-Δt	$\|v\|_\infty$	$\|v\|_2$	$\|w\|_\infty$	$\|w\|_2$	CPU
1	EU-2400	20.6	5.0	2.3×10^{-2}	9.6×10^{-4}	291
2	SL-2400	20.5	4.8	2.2×10^{-2}	9.4×10^{-4}	378
3	SL-7200	20.6	4.8	2.2×10^{-2}	9.6×10^{-4}	226
3b	SL-7200[e]	21.0	4.8	2.2×10^{-2}	9.4×10^{-4}	616
4	SL-1200	20.7	4.8	2.2×10^{-2}	9.3×10^{-4}	527
5	EU-1200	20.9	5.1	2.3×10^{-2}	9.7×10^{-4}	377
6	HNHh-150	20.8	4.6	2.1×10^{-2}	9.1×10^{-4}	1418
7	HNHnh-150	20.7	4.7	2.1×10^{-2}	9.2×10^{-4}	2687
8	ADIprc-150	19.8	4.7	2.1×10^{-2}	9.3×10^{-4}	2043
9	EXPL-1200	20.3	4.6	2.1×10^{-2}	8.9×10^{-4}	704
10	IMPL-1200	20.3	4.6	2.1×10^{-2}	8.9×10^{-4}	437
11	INCM-1200	19.7	4.6	2.1×10^{-2}	9.0×10^{-4}	677
12	ELAS-1200	20.1	4.6	2.1×10^{-2}	9.0×10^{-4}	356

putational effort is already in the elliptic solver, so that overall model efficiency strongly depends on such technical issues as stopping criteria (Smolarkiewicz et al. 1997) and effective preconditioning (Skamarock et al. 1997). We believe that improvement in the latter will lead to further acceleration of the model.

In order to establish the solution dependence on model design and on the numerical scheme employed, as well as on alternate formulations of the governing equations of motion, we have performed a series of simulations like that in Fig. 1. The results of this sensitivity study are summarized in Table 2.

Table 2 collects various runs in a certain logical order as follows. Entries 1–5 are for the semi-Lagrangian and Eulerian runs of the semi-implicit anelastic model (entry 6 in Table 1) at different time steps; run 3b is identical to run 3 except for a tighter convergence criterion (one order of magnitude) in the GCR pressure solver. Entries 6–8 are for the hydrostatic and nonhydrostatic runs using explicit (with respect to internal gravity waves) variants of the semi-Lagrangian anelastic model (entries 2 and 3 in Table 1). Runs 6 and 7 are for the hydrostatic and nonhydrostatic options of the model based on the hydrostatic first guess, and run 8 is for the alternate nonhydrostatic model with an ADI-type preconditioner of the 3D elliptic pressure solver. Since the explicit model runs are prohibitively expensive, further applications of the explicit models (entries 9–12) incorporate a heavy dissipative filter in polar regions[7] to allow a substantially larger time step. Thus, runs 9 and 10 were designed to make the explicit and semi-implicit nonhydrostatic semi-Lagrangian anelastic runs 8 and 4 directly comparable. Finally, entries 11 and 12 collect results of the simulations using alternate governing equations of motion (entries 5 and 4 in Table 1). Run 11 uses the fully nonlinear incompressible Euler equations (4)–(6), and so addresses the impact of the Boussinesq type linearization inherent in the anelastic model (1)–(3). Run 12, in turn, addresses the impact of incompressibility inherent in the anelastic model by admitting a finite speed of sound while retaining the Boussinesq approximation.

TABLE 3. Difference analysis of various runs collected in Table 2.

Runs	$\|\delta v\|_\infty$	$\|\delta v\|_2$	$\|\delta w\|_\infty$	$\|\delta w\|_2$
Δ(3, 4)	3.3	0.79	1.2×10^{-2}	3.8×10^{-4}
Δ(3, 2)	2.8	0.66	1.2×10^{-2}	3.6×10^{-4}
Δ(3, 3*b*)	3.0	0.71	2.3×10^{-3}	8.9×10^{-5}
Δ(1, 2)	2.2	0.49	6.8×10^{-3}	2.6×10^{-4}
Δ(4, 5)	2.3	0.44	6.4×10^{-3}	2.6×10^{-4}
Δ(7, 8)	1.9	0.52	2.2×10^{-3}	1.5×10^{-4}
Δ(6, 8)	1.7	0.52	2.1×10^{-3}	1.6×10^{-4}
Δ(1, 5)	1.5	0.35	4.1×10^{-3}	1.6×10^{-4}
Δ(11, 9)	0.9	0.15	2.1×10^{-3}	1.5×10^{-4}
Δ(2, 4)	0.8	0.19	2.0×10^{-3}	8.7×10^{-5}
Δ(9, 10)	0.9	0.14	2.3×10^{-3}	7.7×10^{-5}
Δ(12, 9)	0.7	0.17	6.6×10^{-4}	6.1×10^{-5}
Δ(6, 7)	0.8	0.06	8.0×10^{-4}	7.6×10^{-5}

For ease of comparison, the table lists L_∞ and L_2 norms of the meridional and vertical velocity fields—natural perturbation fields with respect to the ambient flow (9)—as well as the computational expense of the model measured by the CPU time (in minutes). As illustrated by the values collected in tables, all the listed solutions agree to about 10%. In fact, they are all similar to that shown in Fig. 1 and are hardly distinguishable in the figures. In order to quantify the differences between various experiments, we have performed analyses of the appropriate difference fields. The results are summarized in Table 3.[8]

Table 3 supports a number of interesting conclusions. We draw attention to a few points of special note. In general, the differences due to the higher-order truncation errors of legitimate modes of executing contemporary global models (i.e., various time steps, Eulerian, Lagrangian, various pressure solvers, etc.) overwhelm the differences due to analytic formulation of the governing equations [cf. Nance and Durran (1994) for a similar conclusion in the area of small-scale dynamics]. The largest differences observed are due to the six-fold difference in Δt (using the semi-Lagrangian semi-implicit model), while the smallest differences are between the hydrostatic and nonhydrostatic model formulations.

[7] The Rayleigh friction and Newtonian cooling–heating terms are included, respectively, in the momentum and entropy equations, with the reciprocal of the attenuation timescale increasing linearly from 0 to 1/150 s^{-1} over the five grid intervals near each pole.

[8] Our intention was to order the analyses of the difference fields in the decreasing magnitude of the differences. In some cases, this required a subjective judgement, since not all the norms used decrease at the same rate.

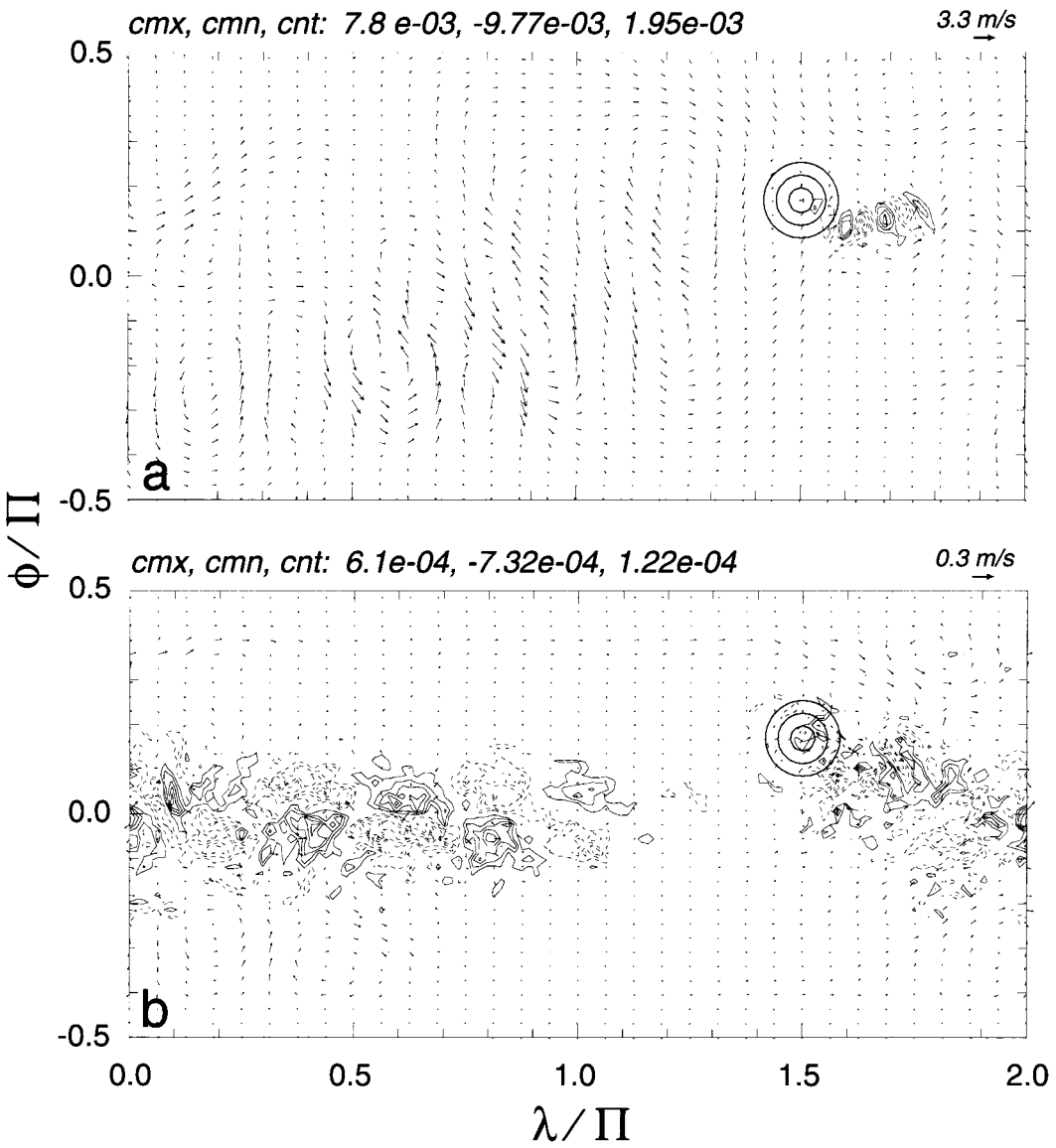

FIG. 2. The vertical velocity difference field δw, with imposed flow difference vectors (δu, δv), for (a) the first $\Delta(3, 4)$ and (b) the last $\Delta(6, 7)$ entry in Table 3. The contouring convention is the same as in Fig. 1.

For illustration, in Fig. 2, we show the respective δw difference fields (cf. plate a in Fig. 1).[9] In particular, note the maximal vertical velocity $\delta w|_{\Delta(6,7)} \sim 10^{-3}$ m s^{-1}; that is, an order of magnitude less than the vertical velocities of the actual flow. The relative overhead of solving the nonhydrostatic problem is ~90% in the model where the nonhydrostatic solution is sought as a perturbation to the hydrostatic result, but only ~44% in the simpler model without the hydrostatic counterpart. For a sufficiently small Δt, the difference between the explicit and implicit $\Delta(9, 10)$ model formulations is small. Note that it is the implicit model that is computationally more efficient, most likely due to the better conditioning of the elliptic pressure operator.

The results collected in Tables 2 and 3 measure the proximity of various numerical solutions, but offer no information about their absolute accuracy (except for the correct magnitude of the vertical velocity). In order to assess the accuracy of approximate solutions (note the lack of the analytic solution), as well as to comment on relative accuracy of semi-Lagrangian and Eulerian versions of the model algorithm, we consider two separate measures. Table 4 lists values of the density-normalized inverse flow Jacobian

[9] The corresponding δv fields are not shown because: (i) they mostly mimic the wave field in Fig. 1b, so the numeric values of the δv norms in Table 3 adequately describe the differences; and (ii) the vectors of the flow difference already give a sense of δv field.

TABLE 4. Density normalized inverse flow Jacobians and the entropy conservation measure for the semi-implicit semi-Lagrangian and Eulerian experiments from Table 2.

Run	Algorithm	Δt	max $\mathcal{J}$	min $\mathcal{J}$	$\|\mathcal{J}-1\|_2$	C
3	SL	7200	1.02	0.380	8.7×10^{-3}	7.7×10^{-6}
2	SL	2400	1.01	0.996	4.6×10^{-4}	3.1×10^{-6}
1	EU	2400	1.00	0.996	3.3×10^{-4}	1.6×10^{-7}
4	SL	1200	1.00	0.998	2.2×10^{-4}	4.1×10^{-6}
5	EU	1200	1.00	0.998	1.7×10^{-4}	5.8×10^{-8}

$$\mathcal{J} \equiv \frac{\rho_o}{\rho} J^{-1} = \frac{\rho_o G(\mathbf{x}_o)}{\rho G(\mathbf{x})} \det\left\{\frac{\partial \mathbf{x}_o}{\partial \mathbf{x}}\right\}, \tag{11}$$

where G is the Jacobian of the coordinate transformation (Smolarkiewicz et al. 1998, 1999). This quantity is readily available only in semi-Lagrangian models. The Lagrangian form of the mass continuity equation, $\rho = \rho_o J^{-1}$, implies that the exact value of $\mathcal{J}$ in (11) should be 1.[10] The quantity $\mathcal{C}$ listed in the last column of Table 4, is defined as

$$\mathcal{C} \equiv \frac{\langle \overline{\rho}\Theta \rangle_t - \langle \overline{\rho}\Theta \rangle_{t=0}}{\langle \overline{\rho}\Theta \rangle_{t=0}}, \tag{12}$$

where $\langle\ \rangle$ denotes the domain integral. Since the selected test problem is fully adiabatic, the exact value of $\mathcal{C}$ is zero. Note, however, that neither semi-Lagrangian nor Eulerian model algorithms assure exact conservation. The semi-implicit design dictates that both models transport Θ' rather than full Θ [cf. Eq. (A3) in the appendix], so even ''conservative'' flux-form Eulerian model contains a residual source of Θ, whose magnitude depends on the accuracy specified for enforcing the anelastic incompressibility constraint (3), via imposing a stopping criterion in the iterative elliptic solver (Smolarkiewicz et al. 1997). In turn, the semi-Lagrangian model is not conservative (i.e., in advective form) by design. The results collected in Table 4 show, in general, that the errors in $\mathcal{J}$ and $\mathcal{C}$ are small, both for semi-Lagrangian and Eulerian options of the model. Except for the semi-Lagrangian simulation with $\Delta t = 7200$ s, maximum errors of the flow Jacobian are less than 0.5%. Conservation errors are clearly smaller for the Eulerian option, and can be reduced even further by imposing a more stringent stopping criterion in the elliptic solver. From the practical viewpoint, however, both model options appear equally viable, at least for this smooth flow case.[11]

[10] In general, for a flow to be realizable (topological), $0 < J < \infty$ [see chapter 2 in Ottino (1989) for a discussion].

[11] In general, the relative efficacy of the semi-Lagrangian and Eulerian approach may be a function of a problem at hand (Bartello and Thomas 1996; Smolarkiewicz and Margolin 1997).

b. Idealized climate states

The orographic planetary flow discussed in the preceding section is fairly laminar and deterministic. The equivalent results generated with many different variants of the model closely match each other, documenting both the hydrodynamic stability of the flow and robustness of the model design. The example considered in this section is very different in nature. Simulations of the idealized climates of Held and Suarez (1994), basically representing thermally forced baroclinic instability on the sphere, bear striking resemblance to large-eddy simulations of convective boundary layers (Nieuwstadt et al. 1992), where small differences in model setups can lead to totally different instantaneous flow realizations, and where different model designs can lead to quite divergent integral flow characteristics. In other words, these simulated flows are both turbulent and stochastic [for illustration, see Fig. 3 in Smolarkiewicz et al. (1999)]. They typify the response of an initially stagnant and uniformly stratified fluid to a diabatic forcing that mimics the long-term thermal and frictional forcing in the earth atmosphere. This diabatic forcing attenuates Θ and $\mathbf{v}$ to the specified equilibrium temperature $\Theta_{\mathrm{EQ}}(|y|, r')$ and $\mathbf{v}|_{r'<z_i} = 0$, where z_i represents a height of the boundary layer (see section 2 in Held and Suarez (1994), for details). The corresponding forcing functions augment the governing equations of motion (1)–(2) with appropriate Rayleigh friction and Newtonian cooling–heating terms.

The original forcing functions of Held and Suarez are expressed in normalized pressure coordinates $\sigma \equiv p/p_s$ (where p_s and p denote, respectively, the full thermodynamic pressures at the surface and in the atmosphere aloft), so their diabatic forcing may evolve in time. In the anelastic model, only gradients of the perturbation pressure are meaningful and the full thermodynamic pressure is, in essence, unavailable. In order to avoid cumbersome procedures attempting to recover the true σ coordinate in our anelastic model, we have simply assumed a standard atmosphere with the density scale of 7 km to evaluate the fixed forcing functions. The significance of such a simplification can be verified easily within the framework of a σ-coordinate model.

In section 3a, we assumed a shallow fluid and used the Boussinesq approximation $\overline{\rho}(z_c) = \rho_o$ and $\overline{\Theta} = \Theta_o$. Here we consider a deep atmosphere and, therefore, solve the anelastic equations (1)–(3) routinely with a variable reference density and potential temperature implied by $N = 10^{-2}$ s^{-1} Brunt–Väisällä frequency assumed for the reference state [cf. section 2b in Clark and Farley (1984)]. The implicit numerical model (entry 6 in Table 1) is employed, and the environmental profiles $\mathbf{v}_e = 0$ and $\Theta_e = \Theta_{\mathrm{EQ}}(\Pi/2, r')$ are assumed. The globe is covered by uniform spherical mesh with $nx \times ny = 64 \times 32$ grid intervals (no grid points at the poles) and the $H = 32 \times 10^3$ m deep atmosphere is resolved with $nz = 40$ uniform grid intervals. The time step of inte-

gration is $\Delta t = 900$ s. The dissipative filter in the polar regions assumes a reciprocal of the attenuation timescale that increases linearly from 0 to 1/86 400 s^{-1} over the four grid intervals near each pole. Also, in lieu of the biharmonic diffusion used in the original Held–Suarez experiments, we exploit the implicit viscosity of the advection algorithms by employing the first-order upwind scheme at every sixth time step of the model (cf. Liska and Wendroff 1998) in both the Eulerian and the semi-Lagrangian simulations.[12] The particular simulation depicted in Fig. 3 used the massively parallel version[13] of the Eulerian model algorithm with the standard and linearized nonoscillatory MPDATA transport schemes for, respectively, Θ' and momenta (Smolarkiewicz and Margolin 1998).

Figure 3 displays the resulting ''climate''; that is, zonally averaged 3-yr means of u and Θ—the data from the first 200 days is excluded. Figure 4 supplements Fig. 3 with equivalent displays of v and w to complete the picture of the simulated climatic circulation. Figure 3 corresponds to the results in Figs. 1 and 2 of Held and Suarez (1994). (Note that their plots are drawn in the σ coordinate.) The agreement of the two solutions is qualitative, which should not be surprising considering the substantial differences between the two models. Our trade winds and equatorial easterlies aloft are somewhat weaker, but our subpolar easterlies are more pronounced. Our westerlies are about as strong but shifted toward the equator. A pronounced neutral stratification in polar regions is an artifact of our filter attenuating local solutions toward Θ_{EQ}, well mixed near the poles, cf. Fig. 1b in Held and Suarez (1994); it is inconsequential for the discussions that follow. Although the Held–Suarez original solutions are for the primitive equations, we do not believe (based on the results of the preceding section) that either hydrostaticity, compressibility, or simplified Coriolis and metric forces are responsible for the differences. Among ''physical'' factors, perhaps the Boussinesq linearization of the pressure gradient terms is important, but even this seems unlikely in the light of the following results.

We have performed numerous experiments to address the sensitivity of Held–Suarez climates to various aspects of the numerical model design. Among these, we have tested sensitivities to the initial and ambient conditions; to the selected reference state; to the definition of the σ-coordinate in the forcing functions; to spatial and temporal resolution; to model depth; to the design, strength, and spatial extent of polar filters; to the various viscosities in the model (in particular, the relative viscosity in the entropy and velocity equations, i.e., Prandtl number); to the flux versus advective (i.e., Eulerian versus semi-Lagrangian) model formulation; and to the linear z versus mass σ (recall $\delta p \sim -\rho\delta z$) vertical coordinate representation. The latter—see Fig. 5, for illustration—has been achieved by an exponential stretching of the vertical coordinate mimicking σ coordinate for the standard atmosphere with the density scale height of 7 km.

We have found that the tropospheric climate is fairly robust, with fine details depending both on the model resolution and characteristics of polar filters. In contrast, the stratospheric solutions are quite sensitive even to the details of the model design.[14] For example, the simulation identical to that summarized in Fig. 3 except for using a somewhat-less viscous option of MPDATA for Θ', results in weaker equatorial easterlies aloft and a slow O(year) meridional oscillation in the stratosphere (cf. Untch 1999). Also, a similar simulation but using semi-Lagrangian advection, produces westerlies whose magnitude increases monotonically with height (no closed jets). However, both models tend to reproduce the solution in Fig. 3 when the model depth is doubled and stretched ''mass'' coordinates are employed with a vertical gravity wave absorber layer at the top of the model. Experiments using enhanced viscosity in the vertical transport terms—a crude convection parameterization—demonstrate another strong sensitivity of the solutions. More such examples could be presented (cf. Boville and Cheng 1988; Boville and Baumhefner 1990; and the references therein).

Tables 5 and 6 quantify and compare selected simulated climates. Table 5 lists extrema and standard deviations of zonal velocity (m s^{-1}) and potential temperature (K), and L_∞ and L_2 norms of meridional, and vertical velocities (m s^{-1}). Experiment EU-dfl is the default run discussed extensively earlier in this section. Run 1 (EU-rfs) assumes a twice-larger Brunt–Väisällä frequency for the reference state but is otherwise identical to the default run, and run 2 (EU-bou) tests the shallow-convection (classical incompressible Boussinesq) approximation with a constant density and potential temperature in the reference state. The latter two experiments address the adequacy of the anelastic approximation. Run 3 (EU-f4b) differs from EU-dfl only by a 10-times weaker polar filter. Run 4 (EU-adv) uses a slightly less viscous MPDATA option for the advection of Θ', and the run 5 (SL-dfl) is identical to EU-dfl but uses the semi-Lagrangian option of the model.

When the difference fields are compared (Table 6), it is apparent that the solutions are more sensitive to details

[12] Our semi-Lagrangian interpolation procedure is built on nonoscillatory advection transport schemes similar to those used in the Eulerian model (Smolarkiewicz and Pudykiewicz 1992; Smolarkiewicz and Grell 1992).

[13] The parallelization strategy adopted in the global model (a single program multiple data message-passing approach with an explicit 2D horizontal grid decomposition) closely follows that used in the small-scale anelastic model (Anderson and Smolarkiewicz 1997; Anderson et al. 1997), a precursor of the present code.

[14] Note that comparisons in z coordinates clearly expose the differences in stratospheric climate, see Fig. 5 for illustration.

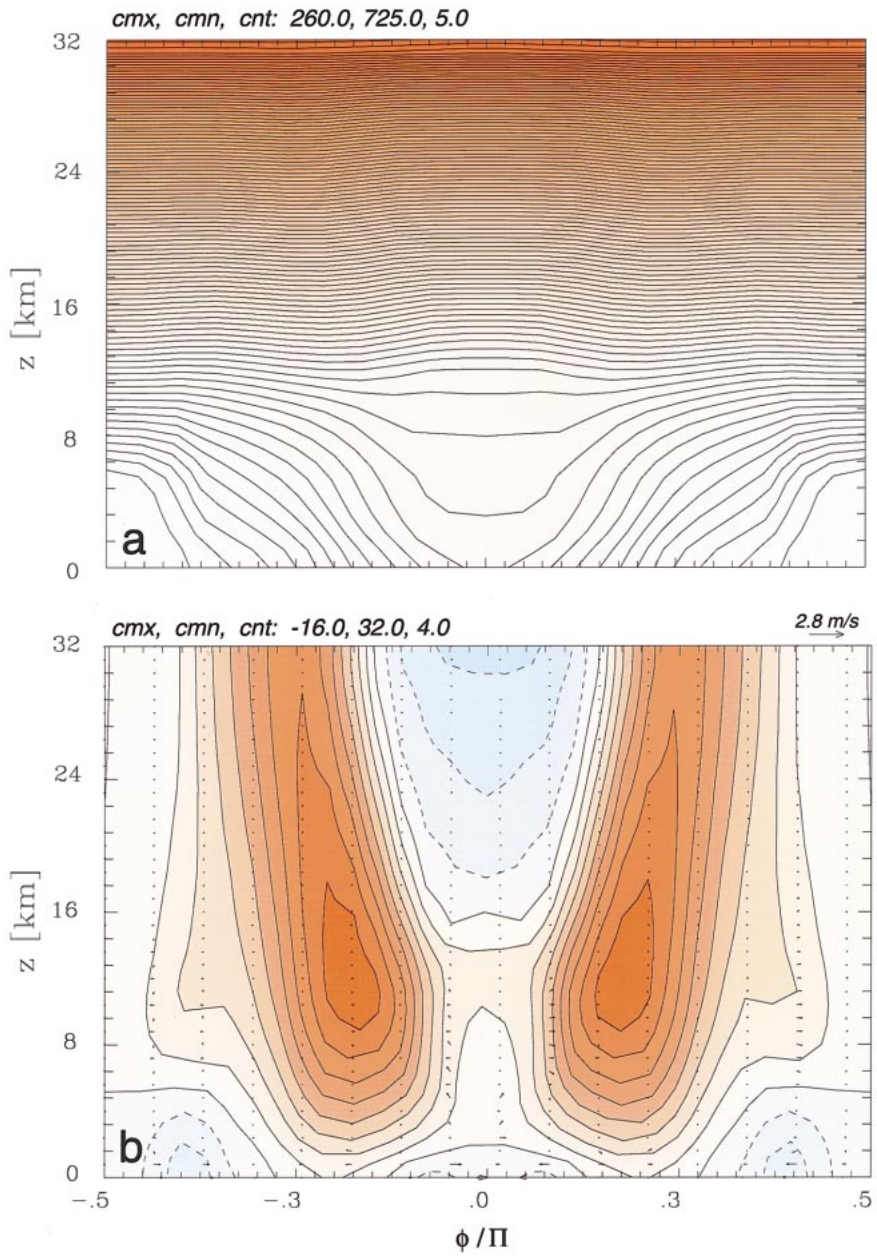

FIG. 3. The zonally averaged 3-yr means of (a) potential temperature and (b) zonal velocity for the simulation of the Held–Suarez idealized climate. Contour extrema and intervals are shown in the upper-left corner of each plate. Negative values are dashed. Maximum vector length is shown in the upper-right corner of (b).

of the numerical schemes than to fairly substantial departures in specific realizations of the anelastic system of the equations. The Boussinesq linearization around the reference state with four-times larger stability—an anelastic model with the stratosphere in focus—affects the resulting climates much less (in terms of standard deviations) than, for example, switching between closely related second-order-accurate semi-Lagrangian and Eulerian advection algorithms. The latter has an even more pronounced effect than making the unjustifiable shallow-convection approximation within the anelastic system (thereby inhibiting the non-Boussinesq amplification of vertically propagating disturbances). The corresponding comparison of the dispersions of mean climatic states indicates a roughly constant range of weather variability for all climatic states (Table 7), whereas an analysis of the respective difference fields of σ^X (not shown) tends to correlate with the results of Table 6.

The picture emerging from our sensitivity study—consistent with other reported results (Chen and Bates

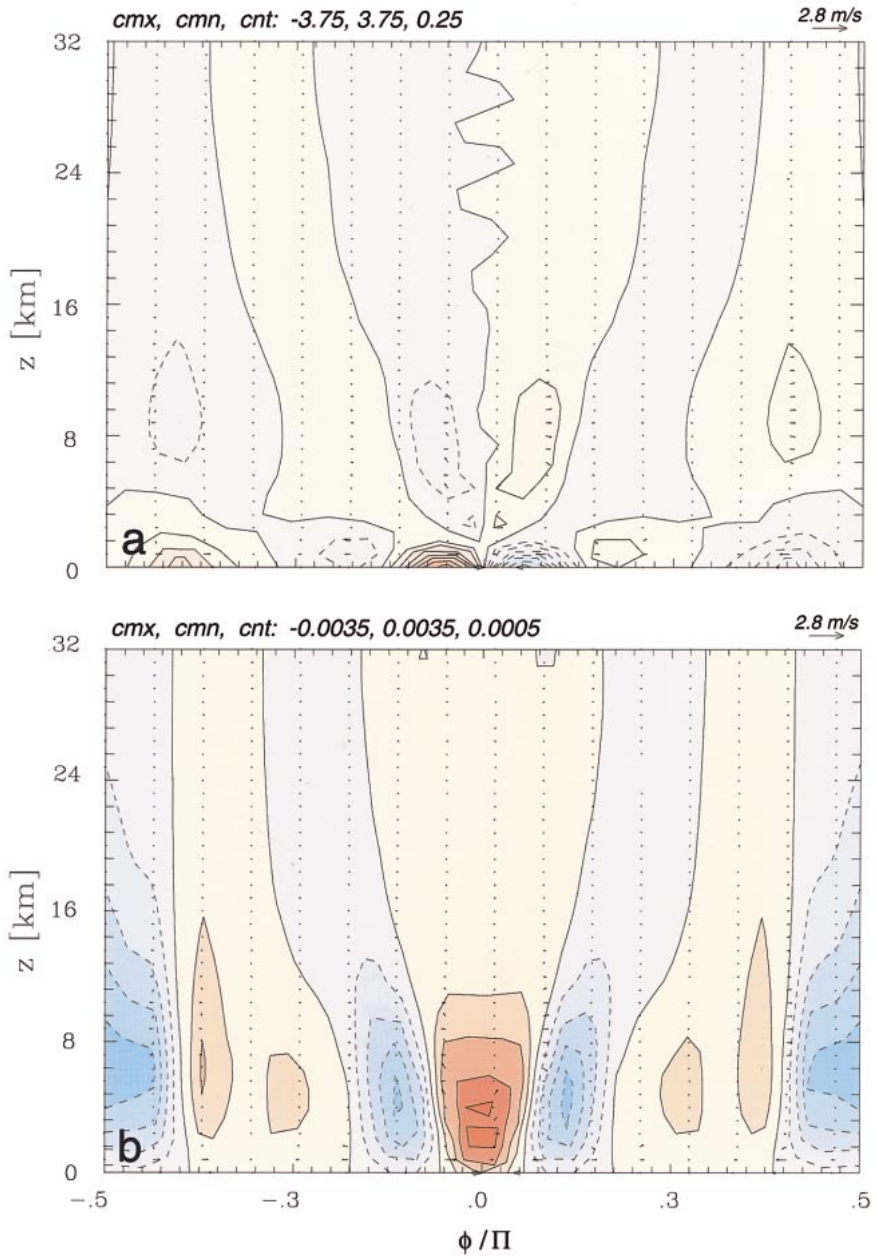

FIG. 4. The zonally averaged 3-yr means of (a) meridional and (b) vertical velocity for the simulation of the Held–Suarez idealized climate. Contouring convention is the same as in Fig. 3.

1996; Untch 1999)—is that the simulated Held–Suarez climates depend strongly on the viscous properties of the numerical models employed (and on subgrid-scale transport, in general), regardless of whether those arise via explicit parameterizations or implicit effects of the truncation errors. In our experience, the *smaller* the viscosity of the model, the *less robust* are the climate simulations. The latter implies the dependence on details of convection parameterizations and, ultimately, the need for resolving convective scales in climate modeling. Direct modeling of clouds on the global scale is beyond the reach of the computational technology perhaps for decades. However, this is where nonhydrostatic global models may be helpful. Less constrained forms of the Navier–Stokes' equations open new research possibilities that would be either cumbersome or even invalid in models based on the primitive equations. For example, the cloud-resolving convection parameterization (Grabowski and Smolarkiewicz 1999) embeds a 2D cloud-resolving model in each column of a large-scale model. There, the compatibility of the governing equations simplifies the formalism of the model cou-

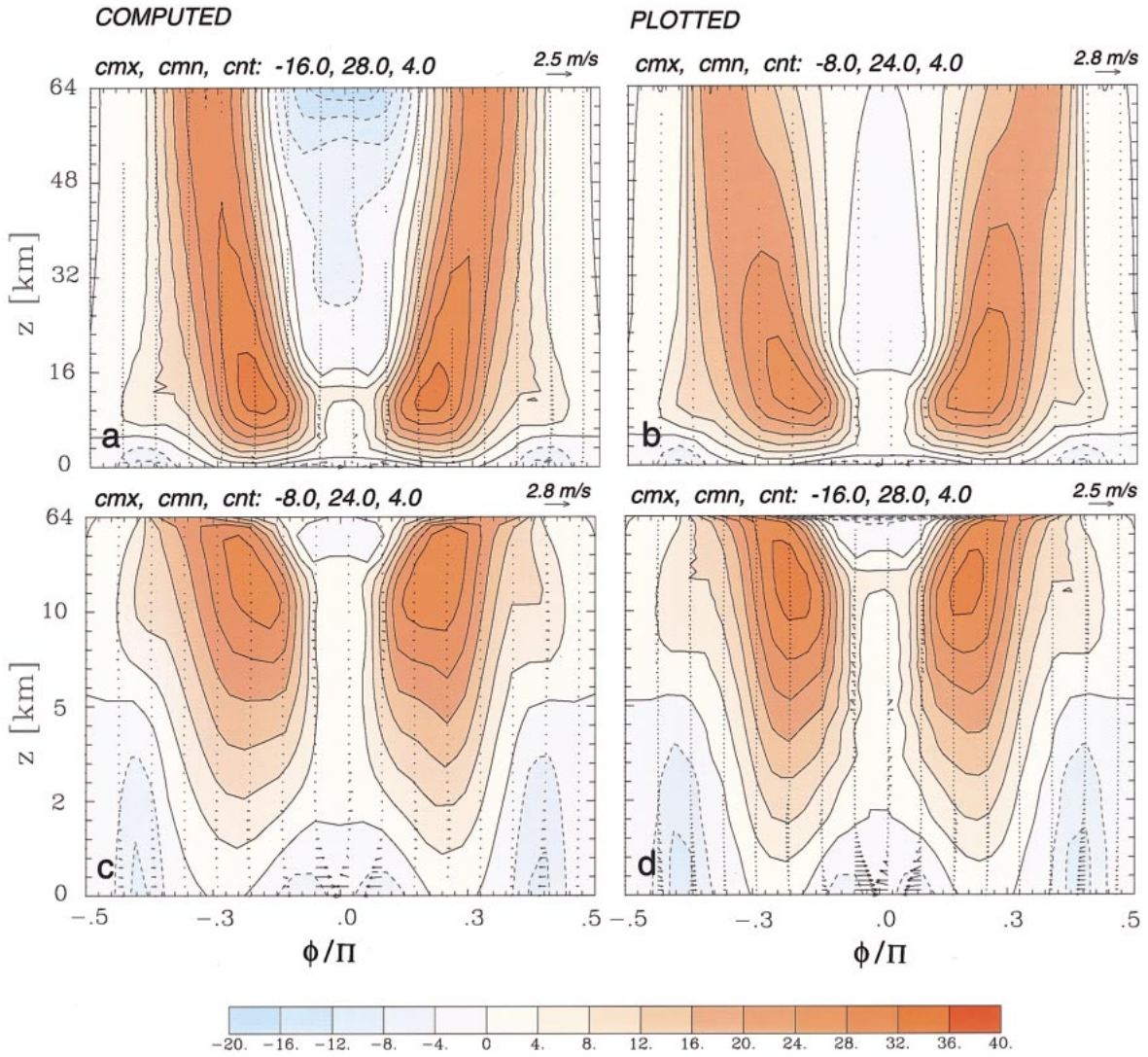

FIG. 5. The zonally averaged 3-yr means of zonal velocity, linear z vs mass σ vertical coordinate representation (note stretched z labels in the lower row). Contouring convention is similar to that used in Fig. 3. The z-coordinate solution displayed in (a) z and (d) σ coordinates. The σ-coordinate solution displayed in (c) σ and (b) z coordinates. The z-coordinate solution uses $nz = 81$ grid points in the vertical with uniform interval $\Delta z = 800$ m. The σ-coordinate solution covers the same model depth with $nz = 41$ stretched levels (see the text for further details).

TABLE 5. Comparison of selected executions of the semi-implicit anelastic model for simulating the idealized Held–Suarez climate. Eulerian model runs 1–4 differ from the default run 0 by, respectively, a modified reference state, Boussinesq approximation, modified polar filter, and altered advection algorithm; run 5 is for the default semi-Lagrangian variant of the model.

Run	Solver	U_{mx}; $U_{mn,}$ U_{sd}	$\lvert V\rvert_{mx}$; V_{sd}	$\lvert W\rvert_{mx}$; W_{sd}	θ_{mx}; θ_{mn}; θ_{sd}
0	EU-dfl	35.3; −16.6; 11.8	2.8; 0.22	3.3×10^{-3}; 7.0×10^{-4}	738.4; 255.1; 141.3
1	EU-rfs	30.2; −10.9; 10.2	2.6; 0.19	3.1×10^{-3}; 6.6×10^{-4}	738.4; 255.1; 141.3
2	EU-bou	36.4; −12.6; 11.4	3.0; 0.24	5.4×10^{-3}; 7.6×10^{-4}	738.9; 255.1; 142.7
3	EU-f4b	35.1; −19.6; 9.8	2.6; 0.16	3.3×10^{-3}; 3.9×10^{-4}	739.2; 260.3; 140.1
4	EU-adv	33.5; −11.0; 9.8	2.6; 0.21	3.0×10^{-3}; 7.3×10^{-4}	739.3; 255.0; 141.5
5	SL-dfl	23.6; −7.7; 8.2	2.0; 0.24	5.6×10^{-3}; 6.7×10^{-4}	738.4; 255.0; 141.7

TABLE 6. Difference analysis of runs collected in Table 5.

Diff.	$\lvert\delta U\rvert_{mx}$; δU_{sd}	$\lvert\delta V\rvert_{mx}$; δV_{sd}	$\lvert\delta W\rvert_{mx}$; δW_{sd}	$\lvert\delta\theta\rvert_{mx}$; $\delta\theta_{sd}$
5-0	17.8; 7.1	1.5; 0.18	3.8×10^{-3}; 4.4×10^{-4}	12.6; 2.2
2-0	20.7; 5.2	1.1; 0.12	3.6×10^{-3}; 3.9×10^{-4}	8.3; 3.2
3-0	13.7; 5.1	0.8; 0.10	1.9×10^{-3}; 4.6×10^{-4}	15.0; 2.9
4-0	24.8; 4.9	0.3; 0.04	6.0×10^{-4}; 1.6×10^{-4}	6.5; 1.9
1-0	11.7; 2.8	0.3; 0.03	4.8×10^{-4}; 8.5×10^{-5}	2.8; 0.8

pling—a common issue in multilevel methods and mesh-refinement schemes. Another example is a series of simulations in Smolarkiewicz et al. (1999), where the Held–Suarez experiments were extended on abstract aquaplanets with radii decreasing successively by a factor of 10. Such rescaled globes cover range of scales unaccessible to primitive equations. In principle, they could be employed to investigate certain effects of small- and mesoscale phenomena on global flows and vice versa at a fundamental level.

4. Summary remarks

In the global atmospheric–oceanic modeling community, there is a trend toward replacing the traditional hydrostatic primitive equations with less constrained nonhydrostatic forms of the Navier–Stokes' equations (Semmazi et al. 1995; Marshall et al. 1997a; Cullen et al. 1997). The few existing nonhydrostatic global models vary in analytic formulation and numerical design, reflecting their different purposes and origins. Drawing from the philosophy of the ''all-scale-research'' ocean model of Marshall et al. (1997a), we have extended our anelastic NFT small-to-mesoscale atmospheric model (broadly documented in the literature) to a mountainous sphere and have dispensed naturally with the traditional meteorological simplifications of hydrostaticity, gentle terrain slopes, and weak rotation.

To assess the impact of the assumptions inherent in the small-scale model on global flows, we have measured relative departures of various variants of the global model (hydrostatic, nonhydrostatic, elastic Boussinesq, anelastic, and incompressible Euler) against the truncation errors of optional (e.g., Eulerian, semi-Lagrangian, implicit, explicit) second-order-accurate discretization approximations. We have performed an extensive analysis for an idealized orographic planetary flow, representative of basic geophysical fluid dynamics of a mechanically forced laminar system. This analysis revealed that the differences due to the higher-order truncation errors of legitimate modes of executing contemporary global models overwhelm the differences due to analytic formulation of the governing equations. For an idealized climate problem, representative of a thermally forced turbulent system, a similar analysis was computationally affordable only within the context of the semi-implicit anelastic model. There, we measured departures of the climates simulated with different anelastic reference states (emphasizing either tropospheric or stratospheric circulations) against the truncation errors. Similar as in the laminar case, we have found that the solutions' departures due to fairly substantial variations in the optional realizations of the anelastic system are smaller than the higher-order truncation errors.

TABLE 7. Variability of instantaneous Held–Suarez flows for corresponding mean states collected in Table 5, as measured with $\sigma^X \equiv [(X - [X])^2]^{1/2}$, where [ ] refers to zonal and temporal averaging.

Run	σ^U_{av}; σ^U_{sd}	σ^V_{av}; σ^V_{sd}	σ^W_{av}; σ^W_{sd}	σ^θ_{av}; σ^θ_{sd}
0	4.0; 1.6	3.9; 2.1	3.2×10^{-3}; 3.2×10^{-3}	2.2; 1.4
1	3.6; 1.5	3.6; 2.1	3.3×10^{-3}; 3.2×10^{-3}	2.3; 1.5
2	3.3; 1.8	2.9; 1.9	1.3×10^{-2}; 8.7×10^{-3}	2.0; 1.5
3	4.1; 1.1	4.0; 1.8	3.4×10^{-3}; 3.7×10^{-3}	2.3; 1.1
4	4.7; 2.0	4.4; 2.1	8.0×10^{-3}; 4.8×10^{-3}	2.8; 1.8
5	4.4; 2.1	3.9; 2.2	5.7×10^{-3}; 6.4×10^{-3}	2.8; 1.8

In general terms, our results document that nonhydrostatic anelastic global models derived from small-scale codes can capture adequately a broad range of planetary flows while requiring relatively minor overhead due to the nonhydrostatic formulation. Since our small-scale models secure no large-scale balances a priori in their analytic–numerical design, this is a success of an ''atomistic'' school of thought in numerical modeling of atmospheres and oceans. In addition to a purely theoretical interest, the adequacy of the anelastic approximation has important practical consequences. The Boussinesq linearization inherent in the anelastic system greatly simplifies the task of designing accurate, flexible, and computationally efficient all-scale-research models for atmospheric circulations. This is especially important within the class of NFT models, where two-time-level self-adaptive nonlinear numerics leads inevitably to difficult nonlinear elliptic problems for implicit discretizations of fully compressible Euler equations.

The semi-implicit nonhydrostatic NFT model presented in this paper is only a first step toward a future ''global cloud model'' intended for studies of the role of small- and mesoscale phenomena in global flows and climate. Full potential of the nonhydrostatic modeling, in general, and of our semi-implicit model, in particuler, becomes more apparent once the moist processes are included.[15] These developments will be reported in the future.

Acknowledgments. Stimulating discussions with James Hack, Darryl Holm, and David Williamson are gratefully acknowledged. Special thanks go to Mitchell Moncrieff, Philip Rasch, and William Skamarock for their personal reviews of this paper. Comments of three anonymous referees helped to improve the manuscript.

[15] For an outline of the moist scheme and associated issues, see Grabowski and Smolarkiewicz (1999) at http://www-pcmdi.llnl.gov/conf/PDE/registered.txt.

National Center for Atmospheric Research is sponsored by the National Science Foundation. Los Alamos National Laboratory is operated by the University of California for the U.S. Department of Energy. This work has been supported in part by the Department of Energy Climate Change Prediction Program research initiative.

APPENDIX

Elliptic Pressure Equations

In order to avoid solving a nonlinear elliptic equation for pressure, the metric forces $\mathcal{M}$ contributing to $\mathbf{F}^{n+1}$ on the rhs of (8) are either approximated explicitly in the spirit of Adams–Bashfort schemes, or the entire subset of (8) corresponding to three components of the momentum equations is iterated with the metric terms lagged behind. In both cases the metric forces enter the rhs of the resulting *linear* elliptic pressure equation. Although the iterative approach requires solving the elliptic equation at each iteration, it is advantageous overall: in the limit, this approach converges to the trapezoidal-rule approximation, which preserves the neutral character of the metric force. With the first guess $\mathcal{M}^{n+1|0} = \mathcal{M}^n$, one iteration suffices for second-order accuracy. In typical applications for flows on the earth, the results are not sensitive to the number of iterations beyond 2, and the overhead associated with two passes through the pressure solver is insignificant, as the second pass requires only a few iterations of the Krylov solver to maintain the accuracy of the first pass.

Keeping the above discussion in mind, we can now proceed with formulation of an elliptic pressure equation. First, let us rewrite (8) in a simplified notation

$$\boldsymbol{\psi} = \boldsymbol{\psi}^* + \mathbf{F}, \tag{A1}$$

where $\boldsymbol{\psi}^*$ is shorthand for the explicit part of the solution, $0.5\Delta t$ has been absorbed in the definition of $\mathbf{F}$, and all grid indices have been dropped as there is no ambiguity. Second, let us distinguish the pressure gradient force from other contributions to $\mathbf{F}$ such as Coriolis force, buoyancy, and gravity wave absorbers [for the latter, see Smolarkiewicz et al. (1998, 1999)]. For momenta, this leads to an alternate form of (A1)

$$\mathbf{v} = \mathbf{v}^* - \mathbf{G}(\pi) + \mathbf{L}\mathbf{v}, \tag{A2}$$

where $\mathbf{G}$ symbolizes a normalized finite-difference gradient operator, $\pi \sim 0.5\Delta t p'$ denotes a normalized pressure variable, and the linear operator $\mathbf{L}$ combines the remaining contributions to $\mathbf{F}$. The explicit part of the solution $\mathbf{v}^*$ always includes the LE($\tilde{\mathbf{v}}$) transport term and the metric-force contribution $\sim\mathcal{M}$. However, the specific finite-difference definitions of $\mathbf{v}^*$, $\mathbf{G}$, π, and $\mathbf{L}$ depend on both the governing system and the overall design (explicit or implicit) of the time-integration scheme.

In models explicit with respect to internal gravity waves, the entropy equations (2) and (5) are integrated prior to the momentum equations. This allows the buoyancy term in (1) and (4) to be evaluated explicitly at $n + 1$ in (8)—in the spirit of Runge–Kutta schemes—and to enter the $\mathbf{v}^*$ term on the rhs of (A2). In the explicit incompressible Euler model, the finite-difference representation of $\mathbf{G}$ is weighted by the reciprocal of ρ, while $\pi = 0.5\Delta t p'$. In the anelastic model implicit with respect to internal gravity waves, the entropy equation (2) is treated in an alternate form

$$\frac{\mathcal{D}\Theta'}{\mathcal{D}t} = -\dot{\mathbf{x}}\boldsymbol{\nabla}\Theta_e, \tag{A3}$$

where $\dot{\mathbf{x}}\boldsymbol{\nabla}$ is the complete convective derivative operator (see Smolarkiewicz et al. 1998, 1999 for details).[16] Consequently, (A3) must be solved simultaneously with the momentum equations. The buoyancy term in (1) is evaluated implicitly at $n + 1$ in (8)—in the spirit of the trapezoidal-rule scheme—and it enters both the $\mathbf{v}^*$ term and the coefficients of the linear $\mathbf{L}$ operator in (A2).

Regardless of the specific definitions employed in (A2), the straightforward algebraic inversion of (A2) with respect to components of $\mathbf{v}$—a benefit of the colocated grid—is common to all models:

$$\mathbf{v} = (\mathbf{I} - \mathbf{L})^{-1}\mathbf{v}^* - (\mathbf{I} - \mathbf{L})^{-1}\mathbf{G}(\pi). \tag{A4}$$

For all anelastic models, the Poisson equation for π follows the mass continuity constraint (3):

$$0 = -\frac{\Delta t}{\overline{\rho}}\mathbf{D}(\overline{\rho}\mathbf{v}) = -\frac{\Delta t}{\overline{\rho}}\mathbf{D}[\overline{\rho}(\mathbf{v}^{**} - \mathbf{G}^*(\pi)], \tag{A5}$$

where $\mathbf{D}$ denotes the finite difference divergence, $\mathbf{v}^{**}$ and $\mathbf{G}^*$ are shorthand for the modified elements of (A4), and the whole equation has been premultiplied by $-\Delta t/\overline{\rho}$.[17] In the incompressible Euler system, the elliptic pressure equation follows similarly from (6), whereas in the Boussinesq elastic model, (A4) is inserted into the discretized form of (7)

$$\frac{\pi - \pi^0}{\Delta t} + \frac{\Delta t}{2}\frac{c_s^2}{\overline{\rho}}\mathbf{D}(\overline{\rho}\mathbf{v}) = 0, \tag{A6}$$

leading to the Helmholtz equation

$$0 = -\frac{\Delta t}{\overline{\rho}}\mathbf{D}[\overline{\rho}(\mathbf{v}^{**} - \mathbf{G}^*(\pi)] - a^2(\pi - \pi^0), \tag{A7}$$

where $\pi^0 \equiv \pi^n$, and $a^2 \equiv 2/(\Delta t c_s^2)$. Although (A5) and

[16] In contrast to more traditional semi-implicit schemes, we implicitly center in time the entire $\dot{\mathbf{x}}\boldsymbol{\nabla}\Theta_e$ term on the rhs of (A3), to assure stable integrations even for rapidly rotating small globes with steep orography—naturally, this is done at the cost of complicating the resulting elliptic pressure equation [see appendix B in Smolarkiewicz et al. (1999) for a complete technical development].

[17] The factor (-1) assures the formal negative-definiteness of the elliptic operator on the lhs of (A5); further normalization by $\Delta t/(\overline{\rho})$ gives the residual errors of (A5) the sense of the divergence of a dimensionless velocity on the grid.

(A7) might be manipulated to more standard forms (e.g., to a linear problem $A\pi = b$), we purposely emphasize the one adopted here. It exposes links to standard projection procedures (Chorin 1968; Clark 1977; Kapitza and Eppel 1992) and to relaxation methods via physical analogies (Birkhoff and Lynch 1984, chapter 4), it simplifies the design of Neuman boundary conditions for π implied by Dirichlet boundary conditions for **v** (Smolarkiewicz and Margolin 1994), and it suggests physically motivated stopping criteria for iterative solvers (Smolarkiewicz et al. 1997).

REFERENCES

Anderson, W. D., and P. K. Smolarkiewicz, 1997: A comparison of high performance Fortran and message passing parallelization of a geophysical fluid model. *Parallel Computational Fluid Dynamics: Algorithms and Results Using Advanced Computers*, P. Shiano, A. Ecer, J. Periaux, and N. Satofuka, Eds., Elsevier Science, 384–391.

——, V. Grubišić, and P. K. Smolarkiewicz, 1997: Performance of a massively parallel 3D non-hydrostatic atmospheric fluid model. *Proc. Int. Conf. on Parallel and Distributed Processing Techniques and Applications*, Las Vegas, NV, CSREA, 645–651.

Bartello, P., and S. J. Thomas, 1996: The cost-effectiveness of semi-Lagrangian advection. *Mon. Wea. Rev.,* **124,** 2883–2897.

Birkhoff, G., and R. E. Lynch, 1984: *Numerical Solutions of Elliptic Problems.* SIAM, 319 pp.

Boville, B. A., and X. Cheng, 1988: Upper boundary effects in a general circulation model. *J. Atmos. Sci.,* **45,** 2591–2606.

——, and D. P. Baumhefner, 1990: Simulated forecast error and climate drift resulting from the omission of the upper stratosphere in numerical models. *Mon. Wea. Rev.,* **118,** 1517–1530.

Chen, M., and J. R. Bates, 1996: A comparison of climate simulations from a semi-Lagrangian and an Eulerian GCM. *J. Climate,* **9,** 1126–1149.

Chorin, A. J., 1968: Numerical solution of the Navier–Stokes equations. *Math. Comput.,* **22,** 742–762.

Clark, T. L., 1977: A small-scale dynamic model using a terrain-following coordinate transformation. *J. Comput. Phys.,* **24,** 186–214.

——, and R. D. Farley, 1984: Severe downslope windstorm calculations in two and three spatial dimensions using anelastic interactive grid nesting: A possible mechanism for gustiness. *J. Atmos. Sci.,* **41,** 329–350.

——, W. D. Hall, and J. L. Coen, 1996: Source code documentation for the Clark-Hall cloud-scale model code version G3CH0l. NCAR Tech. Note NCAR/TN-426 + STR, 175 pp.

Cullen, M. J. P., T. Davies, M. H. Mawson, J. A. James, and S. Coulter, 1997: An overview of numerical methods for the next generation UK NWP and climate model. *Atmos.–Ocean Special,* **35,** 425–444.

Dutton, J. A., 1986: *The Ceaseless Wind.* Dover Publications Inc., 617 pp.

Eisenstat, S. C., H. C. Elman, and M. H. Schultz, 1983: Variational iterative methods for nonsymmetric systems of linear equations. *SIAM J. Numer. Anal.,* **20,** 345–357.

Gal-Chen, T., and R. C. J. Somerville, 1975: On the use of a coordinate transformation for the solutions of the Navier–Stokes equations. *J. Comput. Phys.,* **17,** 209–228.

Gill, A. E., 1982: *Atmosphere–Ocean Dynamics.* Academic Press, 662 pp.

Grabowski, W. W., and P. K. Smolarkiewicz, 1999: CRCP: A cloud resolving convection parameterization for modeling the tropical convecting atmosphere. *Physica D,* **133,** 171–178.

Grose, W. L., and B. J. Hoskins, 1979: On the influence of orography on large-scale atmospheric flow. *J. Atmos. Sci.,* **36,** 223–234.

Held, I. M., and M. J. Suarez, 1994: A proposal for intercomparison of the dynamical cores of atmospheric general circulation models. *Bull. Amer. Meteor. Soc.,* **75,** 1825–1830.

Kapitza, H., and D. Eppel, 1992: The non-hydrostatic mesoscale model GESIMA. Part 1: Dynamical equations and tests. *Beitr. Phys. Atmos.,* **65,** 129–146.

Lipps, F. B., 1990: On the anelastic approximation for deep convection. *J. Atmos. Sci.,* **47,** 1794–1798.

——, and R. S. Hemler, 1982: A scale analysis of deep moist convection and some related numerical calculations. *J. Atmos. Sci.,* **39,** 2192–2210.

Liska, R., and B. Wendroff, 1998: Composite schemes for conservation laws. *SIAM J. Numer. Anal.,* **35,** 2250–2271.

Margolin, L. G., P. K. Smolarkiewicz, and Z. Sorbjan, 1999: Large-eddy simulations of convective boundary layers using nonoscillatory differencing. *Physica D,* **133,** 390–397.

Marshall, J., A. Adcroft, C. Hill, L. Perelman, and C. Heisey, 1997a: A finite-volume incompressible Navier Stokes model for studies of the ocean on parallel computers. *J. Geophys. Res.,* **102** (C3), 5753–5766.

——, C. Hill, L. Perelman, and A. Adcroft, 1997b: Hydrostatic, quasi-hydrostatic, and nonhydrostatic ocean modeling. *J. Geophys. Res.,* **102** (C3), 5733–5752.

Nance, L. B., and D. R. Durran, 1994: A comparison of the accuracy of three anelastic systems and the pseudo-incompressible system. *J. Atmos. Sci.,* **51,** 3549–3565.

Nieuwstadt, F. T. M., P. J. Mason, C.-H. Moeng, and U. Schumann, 1992: Large-eddy simulation of convective boundary-layer: A comparison of four computer codes. *Turbulent Shear Flows 8,* H. Durst et al., Eds., Springer-Verlag, 343–367.

Oliger, J., and A. Sundström, 1978: Theoretical and practical aspects of some initial boundary value problems in fluid dynamics. *SIAM J. Appl. Math.,* **35,** 419–446.

Ottino, J. M., 1989: *The Kinematics of Mixing: Stretching, Chaos, and Transport.* Cambridge University Press, 364 pp.

Prusa, J. M., P. K. Smolarkiewicz, and R. R. Garcia, 1996: On the propagation and breaking at high altitudes of gravity waves excited by tropospheric forcing. *J. Atmos. Sci.,* **53,** 2186–2216.

Rotunno, R., and P. K. Smolarkiewicz, 1995: Vorticity generation in the shallow-water equations as applied to hydraulic jumps. *J. Atmos. Sci.,* **52,** 320–330.

Saad, Y., and M. H. Schultz, 1986: GMRES: A generalized minimal residual algorithm for solving nonsymmetric linear systems. *SIAM J. Sci. Stat. Comput.,* **7,** 856–869.

Semazzi, F. H. M., J.-H. Qian, and J. S. Scroggs, 1995: A global nonhydrostatic semi-Lagrangian, atmospheric model without orography. *Mon. Wea. Rev.,* **123,** 2534–2550.

Skamarock, W. C., P. K. Smolarkiewicz, and J. B. Klemp, 1997: Preconditioned conjugate-residual solvers for Helmholtz equations in nonhydrostatic models. *Mon. Wea. Rev.,* **125,** 587–599.

Smolarkiewicz, P. K., and T. L. Clark, 1986: The multidimensional positive definite advection transport algorithm: Further development and applications. *J. Comput. Phys.,* **67,** 396–438.

——, and G. A. Grell, 1992: A class of monotone interpolation schemes. *J. Comput. Phys.,* **101,** 431–440.

——, and J. A. Pudykiewicz, 1992: A class of semi-Lagrangian approximations for fluids. *J. Atmos. Sci.,* **49,** 2082–2096.

——, and L. G. Margolin, 1993: On forward-in-time differencing for fluids: Extension to a curvilinear framework. *Mon. Wea. Rev.,* **121,** 1847–1859.

——, and ——, 1994: Variational solver for elliptic problems in atmospheric flows. *Appl. Math. Comput. Sci.,* **4,** 527–551.

——, and ——, 1997: On forward-in-time differencing for fluids: An Eulerian/semi-Lagrangian nonhydrostatic model for stratified flows. *Atmos.–Ocean Special,* **35,** 127–152.

——, and ——, 1998: MPDATA: A finite-difference solver for geophysical flows. *J. Comput. Phys.,* **140,** 459–480.

——, V. Grubišić, and L. G. Margolin, 1997: On forward-in-time

differencing for fluids: Stopping criteria for iterative solutions of anelastic pressure equations. *Mon. Wea. Rev.*, **125,** 647–654.
——, ——, and ——, 1998: Forward-in-time differencing for fluids: Nonhydrostatic modeling of rotating stratified flows on a mountaineous sphere. *Numerical Methods for Fluid Dynamics VI,* M. J. Baines, Ed., Oxford Science, 507–513.
——, ——, ——, and A. A. Wyszogrodzki, 1999: Forward-in-time differencing for fluids: Nonhydrostatic modeling of fluid motions on a sphere. *Proc. 1998 ECMWF Seminar on Recent Developments in Numerical Methods for Atmospheric Modelling,* Reading, United Kingdom, ECMWF, 21–43.
Untch, A., 1999: Aspects of stratospheric modelling at ECMWF. *Proc. 1998 ECMWF Seminar on Recent Developments in Numerical Methods for Atmospheric Modelling,* Reading, United Kingdom, ECMWF, 442–453.
Williamson, D. L., J. B. Drake, J. J. Hack, R. Jakob, and P. N. Swarztrauber, 1992: A standard test set for numerical approximations to the shallow water equations on the sphere. *J. Comput. Phys.*, **102,** 211–224.